

# Probing dark matter particles at CEPC

---

**Zuowei Liu,<sup>a,b,c</sup> Yong-Heng Xu<sup>a</sup> and Yu Zhang<sup>d,c</sup>**

<sup>a</sup>*Department of Physics, Nanjing University, Nanjing 210093, China*

<sup>b</sup>*Center for High Energy Physics, Peking University, Beijing 100871, China*

<sup>c</sup>*CAS Center for Excellence in Particle Physics, Beijing 100049, China*

<sup>d</sup>*Institute of Physical Science and Information Technology, Anhui University, Hefei 230026, China*

*E-mail:* [zuoweiliu@nju.edu.cn](mailto:zuoweiliu@nju.edu.cn), [mg1622019@smail.nju.edu.cn](mailto:mg1622019@smail.nju.edu.cn),  
[dayu@nju.edu.cn](mailto:dayu@nju.edu.cn)

**ABSTRACT:** We investigate the capability of the future electron collider CEPC in probing the parameter space of several dark matter models, including millicharged dark matter models,  $Z'$  portal dark matter models, and effective dark matter operators. In our analysis, the monophoton final state is used as the primary channel to detect dark matter models at CEPC. To maximize the signal to background significance, we study the energy and angular distributions of the monophoton channel arising from dark matter models and from the standard model to design a set of detector cuts. For the  $Z'$  portal dark matter, we also analyze the  $Z'$  boson visible decay channel which is found to be complementary to the monophoton channel in certain parameter space. The CEPC reach in the parameter space of dark matter models is also put in comparison with Xenon1T. We find that CEPC has the unprecedented sensitivity to certain parameter space for the dark matter models considered; for example, CEPC can improve the limits on millicharge by one order of magnitude than previous collider experiments for  $\mathcal{O}(1) - 100$  GeV dark matter.

---

## Contents

<b>1</b>	<b>Introduction</b>	<b>1</b>
<b>2</b>	<b>Dark matter models</b>	<b>2</b>
<b>3</b>	<b>Signals and backgrounds</b>	<b>3</b>
3.1	DM signals	3
3.2	SM backgrounds	6
<b>4</b>	<b>Millicharged DM models</b>	<b>9</b>
<b>5</b>	<b><math>Z'</math> portal DM models</b>	<b>12</b>
<b>6</b>	<b>DM effective operators</b>	<b>16</b>
<b>7</b>	<b>Detector cut optimization</b>	<b>18</b>
<b>8</b>	<b>Summary</b>	<b>19</b>

---

## 1 Introduction

Astrophysical observations tell us that the baryonic matter only contributes about 5% of the energy density of the current universe; more than 80% of the matter content consists of unknown dark matter (DM) particles [1]. To investigate the particle nature of DM is one of the pressing issues in new physics studies beyond the standard model (SM). There is a large variety of experiments in which one can probe the DM particle properties, including dark matter direct detection experiments, dark matter indirect detection experiments, and particle colliders. In this paper, we study the capability of the proposed circular electron positron collider (CEPC) in probing various dark matter models.

Three different running modes for CEPC have been proposed [2], including the Higgs factory mode (hereafter the  $H$ -mode) with  $\sqrt{s} = 240$  GeV for the  $e^+e^- \rightarrow ZH$  production and a total luminosity of  $\sim 5.6$  ab $^{-1}$  for seven years, the  $Z$  factory mode (hereafter the  $Z$ -mode) with  $\sqrt{s} = 91.2$  GeV for the  $e^+e^- \rightarrow Z$  production and a total luminosity of  $\sim 16$  ab $^{-1}$  for two years, and the  $WW$  threshold scan (hereafter the  $WW$ -mode) with  $\sqrt{s} \sim 158 - 172$  GeV for the  $e^+e^- \rightarrow W^+W^-$  production and a total luminosity of  $\sim 2.6$  ab $^{-1}$  for one year<sup>1</sup>. The unprecedented luminosity and energy of CEPC will enable physicists to study the unexplored region in both SM and new physics beyond SM.

Besides CEPC, several other future lepton colliders have been proposed, including the International Linear Collider (ILC) [3], the Future Circular Collider of  $e^+e^-$  (FCC-ee)

---

<sup>1</sup>We take  $\sqrt{s} = 160$  GeV for the  $WW$ -mode throughout our analysis.

[4], and the Compact Linear Collider (CLIC) [5]. These new lepton colliders will certainly deepen our understandings about the dark matter or hidden sector (see e.g. [6–27] for some recent studies).

In this work, we investigate the collider signatures of millicharged DM models which have not been studied at CEPC. We further explore the constraining power of CEPC in probing the  $Z'$  portal DM models from the ordinary dark matter channels, as well as from  $Z'$  visible decay searches. We also study the collider signals arising from dark matter models in which dark matter interacts with SM via effective field theory operators. We study the monophoton signatures at CEPC for the DM related processes and the relevant SM processes. The CEPC upper bounds on dark matter processes as well as on the coupling strength are analyzed for the three proposed running modes. We find that CEPC has the potential to probe the parameter space that is currently unexplored by previous experiments in various dark matter models.

The rest of the paper is organized as follows. In section 2, we introduce the dark matter models that are investigated in this paper. In section 3, we study the monophoton signature arising from DM models and from the SM. A set of detector cuts to suppress the SM backgrounds and to maximize the signal-to-background ratio are proposed. We present the results for millicharged models,  $Z'$  portal models, and DM effective operators in section 4, section 5 and section 6 respectively. A preliminary study on automatic optimizations of detector cuts is given in section 7. We summarize our findings in section 8.

## 2 Dark matter models

We consider the following three types of dark matter models: (1) millicharged DM; (2)  $Z'$  portal DM; (3) DM interactions with SM via effective-field-theory (EFT) operators. The interaction Lagrangian of the millicharged DM is given by

$$\mathcal{L} = e\varepsilon A_\mu \bar{\chi} \gamma^\mu \chi, \quad (2.1)$$

where  $\chi$  is a millicharged Dirac DM particle,  $A_\mu$  is the SM photon,  $e$  is the electromagnetic coupling strength, and  $\varepsilon$  is the millicharge. The interaction Lagrangian for the  $Z'$  portal DM model is given by

$$\mathcal{L} = Z'_\mu \bar{\chi} \gamma^\mu (g_V^\chi - g_A^\chi \gamma_5) \chi + Z'_\mu \bar{f} \gamma^\mu (g_V^f - g_A^f \gamma_5) f, \quad (2.2)$$

where  $\chi$  is the Dirac DM,  $f$  is the SM fermion,  $Z'$  is a spin-1 particle that interacts with DM and with SM fermions. We consider both vector and axial-vector couplings between the  $Z'$  boson and fermions. There are a variety of EFT operators that one can introduce to mediate the interaction between DM and the SM particles. Here we consider the following

four-fermion effective field theory operators [8] [10]

$$\begin{aligned}
\mathcal{L} &= \frac{1}{\Lambda_V^2} \bar{\chi} \gamma_\mu \chi \bar{\ell} \gamma^\mu \ell, \\
\mathcal{L} &= \frac{1}{\Lambda_s^2} \bar{\chi} \chi \bar{\ell} \ell, \\
\mathcal{L} &= \frac{1}{\Lambda_A^2} \bar{\chi} \gamma_\mu \gamma_5 \chi \bar{\ell} \gamma^\mu \gamma_5 \ell, \\
\mathcal{L} &= \frac{1}{\Lambda_t^2} \bar{\chi} \ell \bar{\ell} \chi
\end{aligned} \tag{2.3}$$

where  $\chi$  is the Dirac DM,  $\ell$  denotes the SM charged lepton, and the various  $\Lambda$  parameters are the characteristic scales for new physics. Here  $\Lambda_V$  ( $\Lambda_A$ ) is the new physics scale for vector (axial-vector) interaction;  $\Lambda_s$  ( $\Lambda_t$ ) is the scalar interaction which can be obtained with an  $s$ -channel ( $t$ -channel) mediator integrated out. We note in passing that the effective operator approach starts to break down when the momentum transfer becomes comparable to the suppression scale  $\Lambda$ .

### 3 Signals and backgrounds

#### 3.1 DM signals

Typically, dark matter escapes the particle detectors without leaving any directly detectable signal.<sup>2</sup> Thus, in order to detect DM particles in colliders, at least one final state visible particle is required to be produced in association with the final state DM particles. Here we use the monophoton signature to probe the DM models. Fig. (1) shows the Feynman diagrams for the production process of DM particles in association with a single photon in the final state for the millicharged DM models, the  $Z'$  portal DM models, and DM effective operators.

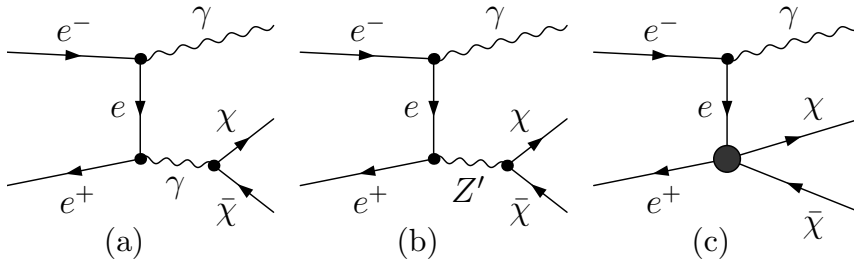


**Figure 1.** Feynman diagrams for the process  $e^+e^- \rightarrow \chi\bar{\chi}\gamma$  in the millicharged DM models (a), in the  $Z'$ -portal DM models (b), and in the DM effective operator formalism (c). Diagrams with photon radiated by the positron are included in the physics analysis but not shown here. The diagrams with photon emitted by the millicharged DM are neglected due to the small  $\varepsilon$  value.

<sup>2</sup>Millicharged particles can be detected with very sensitive detectors; however, for the typical detectors in the high energy colliders, the millicharged particles remain unseen.

For the millicharged DM models, the differential cross section for the  $e^+e^- \rightarrow \chi\bar{\chi}\gamma$  process is given by [28]

$$\frac{d\sigma}{dE_\gamma dz_\gamma} = \frac{8\alpha^3 \varepsilon^2 (1+2y) \beta_\chi}{3sE_\gamma} \left[ \frac{1+x(1+z_\gamma^2)}{1-z_\gamma^2} \right], \quad (3.1)$$

where  $s$  is the center-of-mass energy square,  $m_\chi$  is the DM mass,  $E_\gamma$  is the final state photon energy,  $s_\gamma = s - 2\sqrt{s}E_\gamma$ ,  $y \equiv m_\chi^2/s_\gamma$ ,  $x \equiv E_\gamma^2/s_\gamma$ ,  $\beta_\chi = (1-4y)^{1/2}$ , and  $z_\gamma \equiv \cos\theta_\gamma$  with  $\theta_\gamma$  being the polar angle of the final state photon.

For the  $Z'$  portal DM models where both vector and axial-vector couplings to fermions are present, the production cross section for the process  $e^+e^- \rightarrow \gamma Z' \rightarrow \gamma\chi\bar{\chi}$  is given by

$$\frac{d\sigma}{dE_\gamma dz_\gamma} = \frac{\alpha \left[ (g_V^f)^2 + (g_A^f)^2 \right] \left[ (g_V^\chi)^2 (1+2y) + (g_A^\chi)^2 (1-4y) \right] s_\gamma^2 \beta_\chi}{6\pi^2 s E_\gamma \left[ (s_\gamma - M_{Z'}^2)^2 + M_{Z'}^2 \Gamma_{Z'}^2 \right]} \left[ \frac{1+x(1+z_\gamma^2)}{1-z_\gamma^2} \right], \quad (3.2)$$

where  $M_{Z'}$  is the  $Z'$  mass,  $\Gamma_{Z'}$  is the total  $Z'$  decay width, which is given by

$$\Gamma_{Z'} = \Gamma(Z' \rightarrow \chi\bar{\chi}) + \sum_f \Gamma(Z' \rightarrow f\bar{f}). \quad (3.3)$$

The DM decay width is given by

$$\Gamma(Z' \rightarrow \chi\bar{\chi}) = \frac{M_{Z'}}{12\pi} \sqrt{1 - 4\frac{m_\chi^2}{M_{Z'}^2}} \left[ (g_V^\chi)^2 \left( 1 + 2\frac{m_\chi^2}{M_{Z'}^2} \right) + (g_A^\chi)^2 \left( 1 - 4\frac{m_\chi^2}{M_{Z'}^2} \right) \right]. \quad (3.4)$$

The decay widths into SM fermions can be obtained by substituting the couplings and mass by the SM values. The production cross sections for the DM effective operators can be found in Ref. [10].

The maximum energy that the final state photon can have is given by

$$E_\gamma < \frac{s - 4m_\chi^2}{2\sqrt{s}} \equiv E_\chi^m. \quad (3.5)$$

For the  $Z'$  portal DM models, the monophoton energy spectrum exhibits a resonance centered at the photon energy

$$E_\gamma = \frac{s - M_{Z'}^2}{2\sqrt{s}}, \quad (3.6)$$

with a full-width-at-half-maximum (FWHM) as  $(M_{Z'}/\sqrt{s})\Gamma_{Z'}$ , due to the Breit-Wigner distribution of the  $Z'$  boson. We will refer to such a peak as the “ $Z'$  resonance” hereafter. For the case where  $2m_\chi > M_{Z'}$ , the resonance in the photon energy spectrum exceeds the maximum energy of the final state photon and thus cannot be observed.

In Fig. (2), we compute the total monophoton cross section at CEPC for the three dark matter models, by integrating the differential cross section over the region:  $E_\gamma > 0.1$  GeV and  $|z_\gamma| < 0.99$ . The center-of-mass energy square is  $\sqrt{s} = 240$  (91.2) GeV for the  $H$ -mode ( $Z$ -mode); for the  $WW$ -mode, we use  $\sqrt{s} = 160$  GeV as the benchmark point.

In the millicharged DM model, the monophoton cross section increases when  $\sqrt{s}$  decreases at CEPC, for DM mass lighter than 40 GeV, as shown in the upper-left panel figure

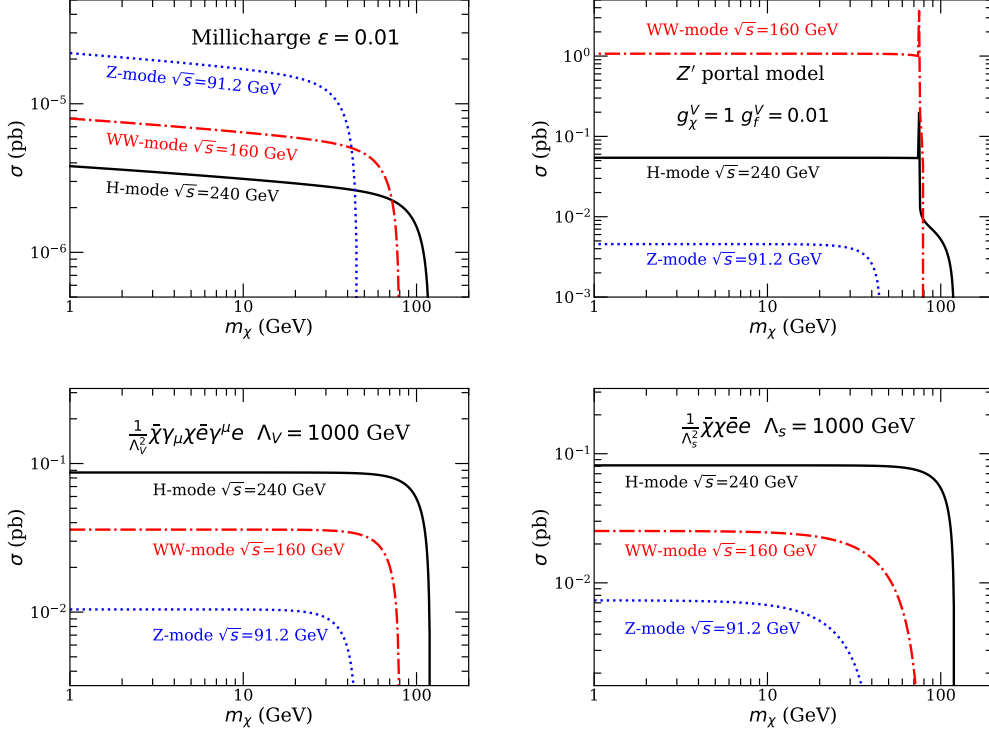


**Figure 2.** Total monophoton cross section  $\sigma(e^+e^- \rightarrow \chi\bar{\chi}\gamma)$  at CEPC in millicharged DM models (upper left panel), in  $Z'$  portal DM models (upper right panel), and with DM effective operators (lower two panels). For the millicharged DM models, we use  $\varepsilon = 0.01$  here. For the  $Z'$  portal DM models, we use  $M_{Z'} = 150$  GeV,  $g_V^f = 0.01$ , and  $g_X^V = 1$  in the vector coupling only case. For the DM effective operators, we use  $\Lambda = 1000$  GeV. The three different running modes are considered here: the  $H$ -mode, the  $Z$ -mode, and the  $WW$ -mode. The monophoton cross sections are computed using the detector cuts:  $E_\gamma > 0.1$  GeV and  $|z_\gamma| < 0.99$ .

of Fig. (2). Thus the  $Z$ -mode has the better sensitivity than the other two modes in probing light millicharged DM. For the four-fermion effective operators, the monophoton cross section increases when  $\sqrt{s}$  increases at CEPC, as shown in the lower two panel figures of Fig. (2). Thus the  $H$ -mode has the better sensitivity than the other two low energy modes in probing the DM effective operators with TeV suppression scale.

For the  $Z'$  portal DM model, we consider the case in which the mass of the  $Z'$  boson is 150 GeV; the monophoton cross section in the  $WW$ -mode is larger than the other two modes, for the case in which DM is lighter than  $\sim 70$  GeV, as shown in the upper-right panel figure of Fig. (2), where we consider the vector coupling only case. It is interesting to note that the monophoton cross section exhibits a resonance feature when the mass of the DM is in the vicinity of  $M_{Z'}/2$ . Thus we expect a better sensitivity in probing the  $Z'$  portal DM models in the  $WW$ -mode, and enhanced constraints in the parameter space where the  $Z'$  boson is nearly twice of the DM mass. We note that the different relations between the total production cross section and  $\sqrt{s}$  in the three types of DM models are primarily due to the mass scale of the mediator.

### 3.2 SM backgrounds

We discuss the major SM backgrounds (BG) at CEPC to the monophoton signature, which include the irreducible background and reducible background.

The irreducible SM background to the monophoton signature at CEPC are the  $e^+e^- \rightarrow \nu_\ell \bar{\nu}_\ell \gamma$  processes, where  $\nu_\ell = \nu_e, \nu_\mu, \nu_\tau$  are the three SM neutrinos. The corresponding Feynman diagrams are displayed in Fig. (3). For muon and tau neutrinos, only  $Z$ -boson diagrams contribute; for the electron neutrino, both  $Z$ -boson diagrams and  $W$ -boson diagrams contribute.

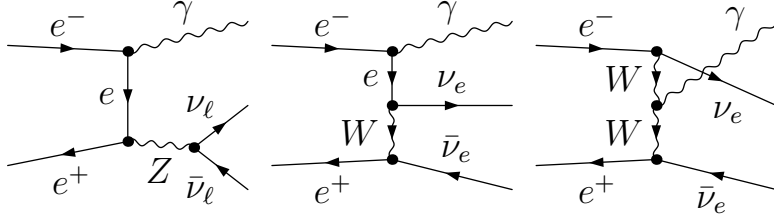


**Figure 3.** Leading order  $e^+e^- \rightarrow \nu \bar{\nu} \gamma$  processes at CEPC. The  $W$ -boson can mediate the  $e^+e^- \rightarrow \nu_e \bar{\nu}_e \gamma$  processes; the  $Z$ -boson diagrams contribute to all neutrino flavors.

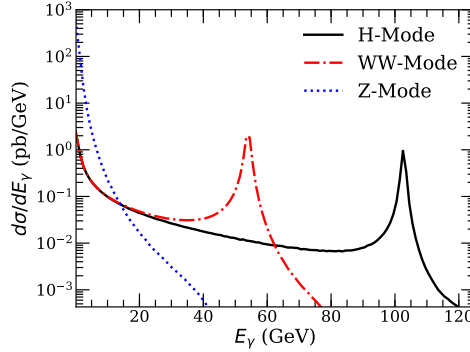


**Figure 4.** Differential cross section for the irreducible standard model background process  $e^+e^- \rightarrow \nu \bar{\nu} \gamma$ . We compute the SM cross sections using FEYNATRS [29] and FORMCALC [30] packages and consider the three CEPC modes with the detector cuts  $E_\gamma > 0.1$  GeV and  $|\cos \theta_\gamma| < 0.99$ .

Due to the SM  $Z$  boson, the irreducible BG exhibits a resonance in the monophoton energy spectrum which is centered at the photon energy

$$E_\gamma^Z = \frac{s - M_Z^2}{2\sqrt{s}} \quad (3.7)$$

with a FWHM as  $\Gamma_\gamma^Z = M_Z \Gamma_Z / \sqrt{s}$ . We will refer to this resonance in the monophoton energy spectrum as the “ $Z$  resonance” hereafter. For the three CEPC running modes, the resonance in the monophoton energy spectrum are located at  $E_\gamma^Z \simeq 103$  GeV with  $\Gamma_\gamma^Z \simeq 0.95$  GeV for the  $H$ -mode,  $E_\gamma^Z \simeq 54$  GeV with  $\Gamma_\gamma^Z \simeq 1.4$  GeV for the  $WW$ -mode (for

$\sqrt{s} = 160$  GeV), and  $E_\gamma^Z \simeq 0$  GeV with  $\Gamma_\gamma^Z \simeq 2.5$  GeV for the  $Z$ -mode. The differential cross section of the monophoton channel due to the SM irreducible background is shown in Fig. (4) where the detector effects have not been taken into account. The  $Z$  resonance features can be easily visualized in the monophoton energy spectrum as shown in Fig. (4). Thus, we will veto the events within  $5\Gamma_\gamma^Z$  at the  $Z$  resonance in the monophoton energy spectrum to suppress the irreducible background contribution.

Next we investigate the reducible background for the monophoton signature at the CEPC. The reducible backgrounds arise due to the limited detection capability of the detectors. Following CEPC CDR [2], we adopt the following parameters for the EMC coverage:  $|\cos\theta| < 0.99$  and  $E > 0.1$  GeV. For the photon energy resolution, we use the resolution in the dual-readout calorimeter [2]

$$\frac{\sigma(E)}{E} = \frac{10.1\%}{\sqrt{E/\text{GeV}}} \oplus 0.4\%. \quad (3.8)$$

We use the above detector parameters in our simulations. The EMC positional resolution has been estimated as  $\sim 0.1$  mm [31], which gives rise to a relative spatial resolution as  $\sim 10^{-5}$ , since the radius of the detector cylinder is about 2 meters. Thus we do not take the spatial resolution into consideration in our simulations due to its smallness.

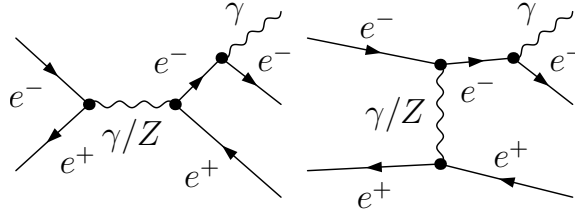


**Figure 5.** Tree level diagrams for the  $e^+e^- \rightarrow e^+e^-\gamma$  processes in SM.

Thus the major reducible SM backgrounds come from the  $e^+e^- \rightarrow \gamma + X$  processes, where only one particle in the final state is visible to the particle detectors which is the final state photon, and  $X$  denotes the other particle (or particles) in the final state that are undetected due to the limitations of the detectors. In SM, the dominate reducible backgrounds include the processes in which  $X = f\bar{f}$  where  $f$  is an SM fermion,  $X = \gamma$ , and  $X = \gamma\gamma$ . The contribution to the monophoton signal from the  $e^+e^- \rightarrow \gamma\gamma$  process is negligible because the CEPC detectors are arranged in a symmetric manner. However, the reducible background from the processes  $e^+e^- \rightarrow f\bar{f}\gamma$  and  $e^+e^- \rightarrow \gamma\gamma\gamma$  can be quite large when the  $f\bar{f}$  and  $\gamma\gamma$  are emitted with  $|\cos\theta| > 0.99$ . For example, due to the collinear singularity, the  $e^+e^- \rightarrow \gamma e^+e^-$  process has large cross section when both final state electron and positron go along the beam directions; the corresponding Feynman diagrams are exhibited in Fig. (5).

To remove the monophoton events in the reducible background, we first compute the energy range of the final state photon for certain emitting angle  $\theta_\gamma$ . Below we take the  $e^+e^- \rightarrow \gamma e^+e^-$  as an example. We define the polar angle  $\theta_b$  such that  $|\cos\theta_b| = 0.99$  corresponds to the boundary of the EMC. For certain polar angle  $\theta_\gamma$ , the maximum energy



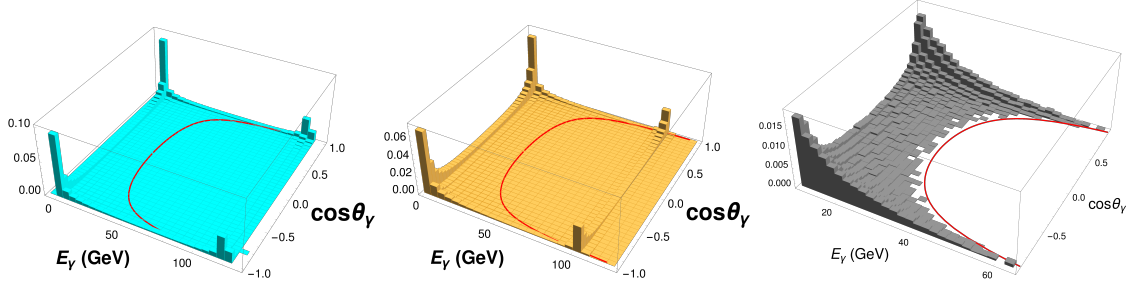


**Figure 6.** Photon  $E_\gamma - \cos\theta_\gamma$  distributions in millicharged models  $e^+e^- \rightarrow \chi\bar{\chi}\gamma$  (left) with  $m_\chi = 1$  GeV and  $\varepsilon = 0.01$ , in SM irreducible BG  $e^+e^- \rightarrow \nu\bar{\nu}\gamma$  (center), and in SM reducible BG  $e^+e^- \rightarrow e^+e^-\gamma$  (right).  $\sqrt{s} = 240$  GeV is used here. The red curves on each plot indicate the kinematic relation  $E_\gamma = E_B^m = \sqrt{s}(1 + \sin\theta_\gamma/\sin\theta_b)^{-1}$  where  $\cos\theta_b = 0.99$ . The  $E_\gamma - \cos\theta_\gamma$  region on the right panel plot is  $E_\gamma > 10$  GeV &  $|\cos\theta_\gamma| < 0.9$ , which is different from the first two plots.

of the photon  $E_\gamma^m$  in the reducible background occurs when the electron and positron emit along different beam directions with  $\theta_{e^\pm} = \theta_b$  and have transverse momenta  $p_T^{e^\pm}$  opposite to the photon transverse momentum  $p_T^\gamma$ . By using momentum conservation in the transverse direction and energy conservation, we obtain  $E_\gamma^m \sin\theta_\gamma = (\sqrt{s} - E_\gamma^m) \sin\theta_b$ , which leads to the maximum photon energy as a function of its polar angle as

$$E_\gamma^m = \sqrt{s} \left[ 1 + \frac{\sin\theta_\gamma}{\sin\theta_b} \right]^{-1} \equiv E_B^m(\theta_\gamma). \quad (3.9)$$

When  $\sin\theta_\gamma = 1$ ,  $E_B^m(\theta_\gamma)$  achieves its minimum value  $(E_B^m)_{\min} \simeq 0.12\sqrt{s}$ . For the three CEPC running modes, the minimum value of  $E_\gamma^m(\theta_\gamma)$  (at  $\theta_\gamma = \pi/2$ ) in the reducible BG is  $\sim 29$  (19, 11) GeV for the  $H$  ( $WW$ ,  $Z$ ) mode respectively. We thus adopt the detector cut  $E_\gamma > E_B^m(\theta_\gamma)$  on the final state monophoton in our analysis to suppress the events arising from the SM reducible backgrounds, such as the  $e^+e^- \rightarrow f\bar{f}\gamma$  and  $e^+e^- \rightarrow \gamma\gamma\gamma$  processes. The right panel figure of Fig. (6) shows that the above cut is efficient in removing the reducible backgrounds.

Thus, to suppress the contributions from SM, we apply the following detector cuts to the monophoton events in SM and in DM models:

- (1)  $E_\gamma > 0.1$  GeV,
- (2)  $|\cos\theta_\gamma| < |\cos\theta_b| = 0.99$ ,
- (3)  $E_\gamma < E_\chi^m = (s - 4m_\chi^2)/(2\sqrt{s})$ ,
- (4) veto  $E_\gamma \in (E_\gamma^Z \pm 5\Gamma_\gamma^Z)$ ,
- (5)  $E_\gamma(\theta_\gamma) > E_B^m(\theta_\gamma) = \sqrt{s}(1 + \sin\theta_\gamma/\sin\theta_b)^{-1}$ .

We will collectively refer to the five detector cuts in the list as the “basic detector cuts” hereafter. Unlike the other detector cuts, the last detector cut in the list is a 2D cut which is applied to the two-dimension space spanned by  $E_\gamma$  and  $\theta_\gamma$ . Both  $E_\gamma^Z$  and  $\Gamma_\gamma^Z$  in the 4th detector cut are functions of  $\sqrt{s}$  in the CEPC running modes.

## 4 Millicharged DM models

In this section, we study the monophoton signatures arising from the millicharged DM models. We use FEYNATRS [29] and FORMCALC [30] packages to compute the differential cross sections in the millicharged models and in the standard model, which are then further smeared using our own code to take into account the photon energy resolution.

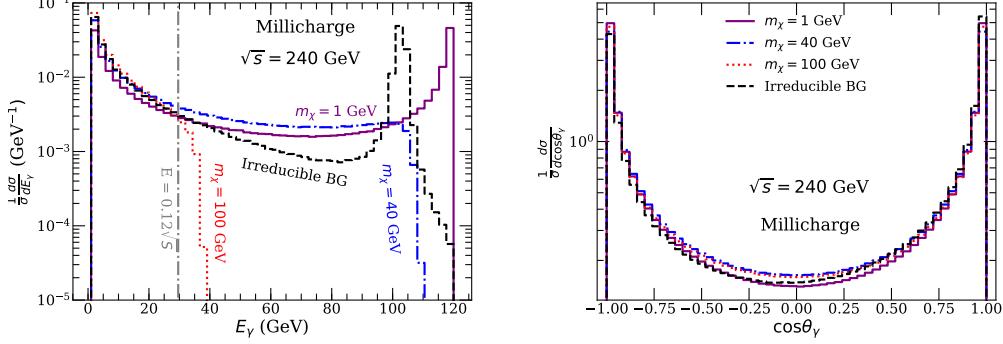


**Figure 7.** Normalized  $E_\gamma$  (left) and  $\cos\theta_\gamma$  (right) distributions for the  $e^+e^- \rightarrow \chi\bar{\chi}\gamma$  processes in millicharged DM models, and for the  $e^+e^- \rightarrow \nu\bar{\nu}\gamma$  processes in SM. Events in 50 bins with equal width on both plots are computed in the CEPC  $H$ -mode ( $\sqrt{s} = 240$  GeV) with detector cuts:  $E_\gamma > 0.1$  GeV and  $|\cos\theta_\gamma| < 0.99$ . For the millicharged models, we consider three different masses:  $m_\chi = 1$  GeV, 40 GeV, and 100 GeV for  $\varepsilon = 0.01$ . The photon energy bin width on the left panel figure,  $\sim 2.4$  GeV, is larger than the photon energy resolution which is  $\delta E_\gamma \simeq 1$  (0.3, 0.1) GeV for  $E_\gamma = 100$  (10, 1) GeV, according to Eq. (3.8). The vertical line  $E = 0.12\sqrt{s}$  indicates the boundary of the detector cut designed to remove the reducible backgrounds.

Fig. (7) shows the normalized  $E_\gamma$  and  $\cos\theta_\gamma$  distributions for the signal process  $e^+e^- \rightarrow \chi\bar{\chi}\gamma$  in the millicharged DM models, and for the irreducible background  $e^+e^- \rightarrow \nu\bar{\nu}\gamma$  in the SM, in the CEPC  $H$ -mode with the detector cuts:  $E_\gamma > 0.1$  GeV and  $|\cos\theta_\gamma| < 0.99$ . Fig. (8) shows the normalized  $E_\gamma$  distributions of the signal and background in the  $Z$ -mode and in the  $WW$ -mode, with the detector cuts:  $E_\gamma > 0.1$  GeV and  $|\cos\theta_\gamma| < 0.99$ .

The millicharged DM models have different monophoton energy distributions for different DM masses. In all the three CEPC modes, the monophoton spectrum shows a peak structure towards the last energy bins, for the case where  $m_\chi = 1$  GeV. Whereas for higher DM masses, the monophoton spectrum steadily decreases with the increment of  $E_\gamma$  and drops rapidly near the termination point  $E_\chi^m = (s - 4m_\chi^2)/(2\sqrt{s})$ .

The SM irreducible background exhibits different energy spectrum from the millicharged DM models. As shown in the left panel figure of Fig. (7), the  $Z$  resonance in the  $H$ -mode is located at  $E_\gamma^Z \simeq 103$  GeV with  $\Gamma_\gamma^Z \simeq 0.95$  GeV. As shown in the right panel figure of Fig. (8), the  $Z$  resonance in the  $WW$ -mode occurs at  $E_\gamma^Z \simeq 54$  GeV with  $\Gamma_\gamma^Z \simeq 1.4$  GeV. The  $Z$  resonance in the monophoton spectrum both in the  $H$ -mode and in the  $WW$ -mode can be easily distinguished from the DM models. In the contrary, the  $Z$  resonance in the  $Z$ -mode appears at  $E_\gamma^Z \simeq 0$  GeV with  $\Gamma_\gamma^Z \simeq 2.5$  GeV, which coincides with the low energy divergence behavior in the millicharged models, as shown in the left panel figure of Fig.

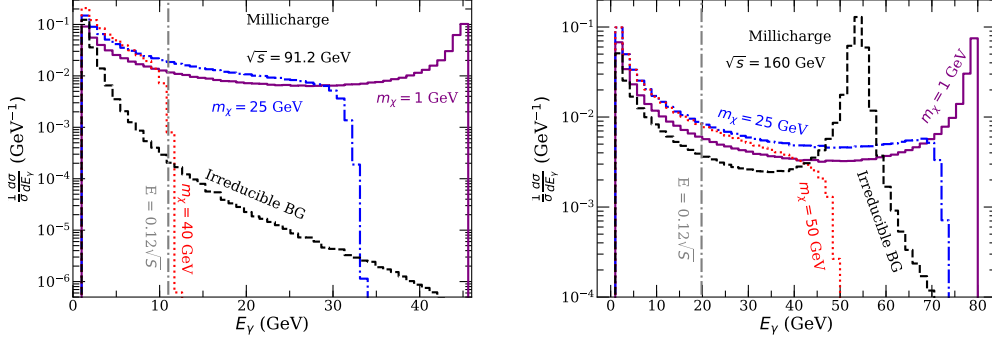


**Figure 8.** Normalized  $E_\gamma$  distribution in the  $Z$ -mode (left) and in the  $WW$ -mode (right), for both the  $e^+e^- \rightarrow \chi\bar{\chi}\gamma$  processes in millicharged DM models and the  $e^+e^- \rightarrow \nu\bar{\nu}\gamma$  processes in SM. Events in 50 bins on both plots are computed with detector cuts:  $E_\gamma > 0.1$  and  $|\cos\theta_\gamma| < 0.99$ . For the millicharged models, we consider  $\varepsilon = 0.01$  for three different masses in each case; we consider  $m_\chi = 1$  GeV, 25 GeV, and 40 GeV in the  $Z$ -mode, and  $m_\chi = 1$  GeV, 25 GeV, and 50 GeV in the  $WW$ -mode.

(8). However, photon events with energy  $E_\gamma \lesssim 0.12\sqrt{s}$  are excluded in the analysis by the detector cut to remove the reducible SM background<sup>3</sup>. In the  $Z$ -mode, because the background events are highly focused in lower  $E_\gamma$  region, as displayed in the left panel figure of Fig. (8) and in Fig. (9), the SM background can be suppressed more efficiently as compared to the other CEPC modes. Thus, in all the CEPC modes, removing the  $Z$  resonance generally increases the capability of probing millicharged DM models.

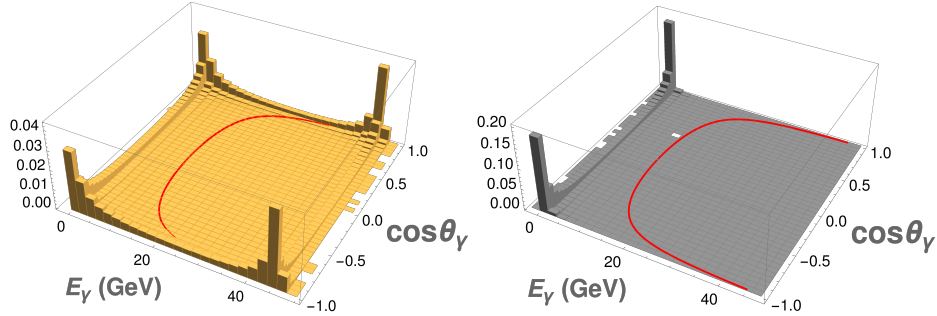


**Figure 9.** Monophoton distributions in the  $E_\gamma$ - $\cos\theta_\gamma$  plane in millicharged DM models (left) and in SM irreducible background (right). Events on both plots are computed in the CEPC  $Z$ -mode. For the millicharged model, we use  $m_\chi = 1$  GeV and  $\varepsilon = 0.01$ . The red curves on both plots indicate  $E_B^m(\theta_\gamma)$  as given in Eq. (3.9).

In the analysis, we employ the basic detector cuts discussed in last section to remove the monophoton events in the reducible background, the SM  $Z$  resonance in the irreducible

<sup>3</sup>In the  $Z$ -mode, the minimum energy cut for the reducible background  $E_\gamma \gtrsim 0.12\sqrt{s} \simeq 11$  GeV exceeds the maximum photon energy in the case where  $m_\chi = 40$  GeV in the millicharged DM models. Thus, to optimize the sensitivity to millicharged DM models beyond  $m_\chi \sim 40$  GeV, one has to relax the detector cut that is designed to eliminate the SM reducible background. We leave this to a future study.

background, and the phase space where DM is unable to reach. Because the millicharged DM models exhibit similar angular distributions as the SM irreducible background in the monophoton channel, as shown in the right panel figure of Fig. (7), we do not impose any further detector cut on  $\theta_\gamma$  beyond the basic detector cuts. Because the monophoton spectrum exhibits a resonance feature near the end of the energy spectrum for the light DM masses, the signal significance can be enhanced in the  $H$  and  $WW$  modes if we only select the monophoton events on the right hand side of the  $Z$  resonance. Thus, to improve the sensitivity in the  $H$ -mode ( $WW$ -mode), we impose the detector cut  $E_\gamma > E_\gamma^Z(s) + 5\Gamma_\gamma^Z(s)$  in addition to the basic detector cuts, for  $m_\chi < 25$  (30) GeV.

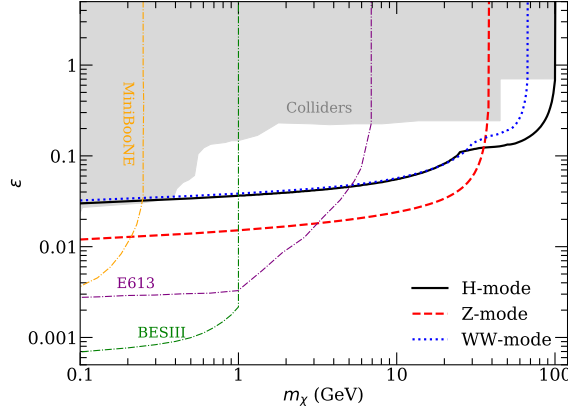


**Figure 10.** Expected 95% CL upper bounds on millicharge with  $5.6 \text{ ab}^{-1}$  data in the  $H$ -mode (black-solid), with  $16 \text{ ab}^{-1}$  data in the  $WW$ -mode (blue-dotted), and with  $2.6 \text{ ab}^{-1}$  data in the  $Z$ -mode (red-dashed). Previous collider bounds are shown as the gray shaded region [32]; expected sensitivity studied in previous analyses are also shown for comparison, including E613 [33], Mini-BooNE [34], and BESIII [28].

To study the 95% C.L. upper bound on the production cross section in new physics models, and consequently on  $\varepsilon$  in millicharged DM models, we use the simple criteria  $N_S/\sqrt{N_B} = 2$  to compute the reach throughout our analysis. Fig. (10) shows the 95% C.L. upper bound on millicharge  $\varepsilon$  as the function of the DM mass  $m_\chi$  in the millicharged DM model. Here we compute the limits based on  $5.6 \text{ ab}^{-1}$  data in the  $H$ -mode,  $16 \text{ ab}^{-1}$  data in the  $WW$ -mode, and  $2.6 \text{ ab}^{-1}$  data in the  $Z$ -mode. The  $Z$ -mode has the best sensitivity for DM mass  $\lesssim 40 \text{ GeV}$ , due to the fact that the production cross section in the millicharged DM model is larger and the SM irreducible background is smaller in the  $Z$ -mode than the other two modes. For the case where DM mass is  $5 \text{ GeV}$ , millicharge  $\sim 0.02$  can be probed by the  $Z$ -mode running of CEPC. The  $H$ -mode has the best sensitivity for DM mass larger than  $40 \text{ GeV}$ . For the case where DM mass is  $\sim 50 \text{ GeV}$ , millicharge  $\sim 10^{-1}$  can be probed by the  $H$ -mode running of CEPC. The CEPC can probe a vast region of the parameter space that is previously unexplored, in the millicharged DM models for DM mass from  $1 \text{ GeV}$  to  $100 \text{ GeV}$ . Compared to previous collider bounds, the improvement on constraints on millicharge is about one order of magnitude for the mass from  $1 \text{ GeV}$  to  $100 \text{ GeV}$ .

The parameter space of millicharged DM to be probed in CEPC,  $\varepsilon \lesssim (0.01 - 0.1)$  for (1-100) GeV mass, has been excluded by many orders of magnitude due to the interaction between the millicharged DM with the CMB [35]. However, if only a small fraction of DM is millicharged (denoted as  $f_{\text{mcp}}$ ), the very stringent CMB constraints can be avoided [36] [37]; the millicharged DM component would be misinterpreted as baryons in the current CMB data. Using Planck data, Ref. [38] put an upper bound on the millicharged DM relic density,  $\Omega_{\text{mcp}} h^2 < 0.001$ . Recently, EDGES experiment [39] observed a stronger absorption signal than expected in the 21 cm data near redshift  $z = 17$ ; many works have studied whether one can use millicharged DM to explain such an anomaly while satisfying various constraints [40–46]. In order to provide the sufficient cooling needed for the 21 cm anomaly, the millicharged DM particle should be in  $\sim \text{MeV}$  scale assuming  $f_{\text{mcp}} \lesssim 1\%$  [40]. Recent studies have further reduced the upper bound on the millicharged DM component:  $f_{\text{mcp}} < 0.6\%$  from helium fraction in the CMB [47]; refs. [44, 45] found if  $f_{\text{mcp}} < 0.4\%$ , the bound from current CMB data can be evaded.

Although astrophysical processes can yield very strong limits on millicharged DM, such analysis often relies on astrophysical assumptions of the millicharged particles. The collider constraints analyzed here with CEPC, however, do not make any astrophysical assumptions about the millicharged particles. Thus, the CEPC constraints given in this analysis for millicharged particles are usually more robust than many of those obtained in astrophysical processes.

## 5 $Z'$ portal DM models

We study in this section the potential constraints on the fermionic DM that interacts with the standard model sector via a  $Z'$  portal. In our analysis, we select the model where  $M_{Z'} = 150 \text{ GeV}$  as the benchmark point. The  $Z'$  boson can interact with fermions via both vector and axial-vector couplings; for simplicity, in this study, only the situations in which  $Z'$  couples to both SM fermions and DM in a pure vector manner ( $g_A = 0$ ), or in a pure axial-vector manner ( $g_V = 0$ ) are considered. To search for the collider signals from the  $Z'$  portal DM model, we study the monophoton signature as well as visible decay from the  $Z'$  boson, in this section.

The normalized monophoton energy distributions in the  $Z'$  portal DM models where  $M_{Z'} = 150 \text{ GeV}$  are shown in Fig. (11), along with the SM irreducible background  $e^+e^- \rightarrow \nu\bar{\nu}\gamma$ . Unlike the millicharged DM models, the monophoton spectrum in the  $Z'$  portal DM models exhibits a peak at  $E_\gamma \simeq (s - M_{Z'}^2)/(2\sqrt{s})$ , which is  $\sim 73 \text{ GeV}$  for the model considered here in the  $H$ -mode. Such a  $Z'$  resonance is visible in Fig. (11) for the  $m_\chi = 1 \text{ GeV}$  and  $m_\chi = 50 \text{ GeV}$  cases; for the  $m_\chi = 100 \text{ GeV}$  case, however, the  $Z'$  resonance can not appear because it exceeds the maximum photon energy in the final state,  $E_\chi^m$ , which is  $\sim 37 \text{ GeV}$  here.

Here we focus our analysis primarily on the  $H$ -mode. This is due to the fact that the 150 GeV  $Z'$  can only be produced off-shell in the  $Z$ -mode. Although the 150 GeV  $Z'$  can be produced on-shell in the  $WW$ -mode, the final state photons from the on-shell  $Z'$  have  $E_\gamma \sim 10 \text{ GeV}$  which falls below the detector cut for the reducible background  $0.12\sqrt{s}$ . Thus for

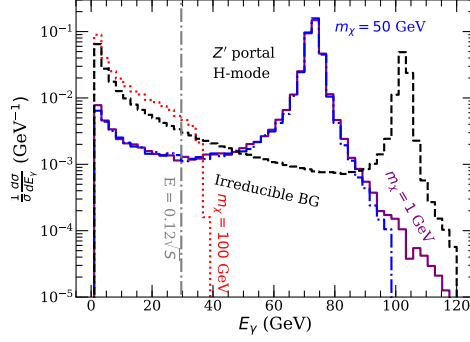


**Figure 11.** Normalized  $E_\gamma$  distribution at the CEPC  $H$ -mode, in the  $Z'$  portal model, as well as in the SM irreducible background process. Only the vector couplings are considered, i.e.,  $g_A^\chi = 0$  and  $g_A^f = 0$ . We use  $g_V^\chi = 1$ ,  $g_V^f = 0.01$ , and  $M_{Z'} = 150$  GeV for the  $Z'$  portal model. For the DM mass, we consider three different cases:  $m_\chi = 1$  GeV, 50 GeV, and 100 GeV.

the  $Z$  mode, we only apply the basic detector cuts; for the  $WW$  and  $H$ , additional detector cuts are applied to maximize the CEPC sensitivity. For the  $WW$  mode, we further veto events with  $E_\gamma > E_\gamma^Z - 5\Gamma_Z$  on top of the basic detector cuts. For the  $H$  mode, we always select events in the  $Z'$  resonance if it is present; thus for  $m_\chi \leq 75$  GeV in the  $H$  mode, we require  $147 \text{ GeV} < M_\gamma < 153 \text{ GeV}$  where  $M_\gamma = \sqrt{s - 2\sqrt{s}E_\gamma}$ .

We can also search for the  $Z'$  boson via its visible decay channels at CEPC (see e.g., [15] [24] for previous studies on this topic). We take the  $\mu^+\mu^-$  final state as the visible channel to probe the  $Z'$  portal DM models in this section. We adopt the muon momentum resolution as follows

$$\frac{\delta p_T}{p_T} = \frac{p_T}{10^5 \text{ GeV}} \bigoplus 0.1\% \text{ for } |\eta| < 1.0 \quad (5.1)$$

and 10 times greater for  $1.0 < |\eta| < 3.0$ , which has been implemented in the CEPC card in Delphes [48]. The muon momentum resolution is much better than the photon energy resolution, as given in Eq. (3.8).

We reconstruct the  $Z'$  boson resonance in the monophoton channel as well as in the  $\mu^+\mu^-$  channel, in Fig. (12). The detector simulations are carried out in MadGraph [49], Pythia 8 [50], and Delphes 3 [48] for both channels. For the monophoton channel, the  $Z'$  resonance is reconstructed via  $M_\gamma = \sqrt{s - 2\sqrt{s}E_\gamma}$ ; for the dimuon channel, the  $Z'$  resonance is reconstructed via the invariant mass of the muon pair. The mass resolution in the monophoton channel can be computed as  $\delta M_\gamma = (\sqrt{s}/M_\gamma)\delta E_\gamma$  which is about 1.5 GeV for  $M_\gamma = 150$  GeV. For the  $Z'$  resonance in the di-muon invariant mass reconstruction, we apply the resolution given in Eq. (5.1) for  $p_T \simeq 50$  GeV to energy, transverse momentum, and longitudinal momentum for each muon, and estimate the mass resolution to be  $\simeq 0.2$  GeV for  $M_{\mu^+\mu^-} = 150$  GeV. We thus use 1.5 (0.2) GeV as the width in the mass reconstruction to bin the events from the monophoton (dimuon) channel, in Fig. (12).

Two benchmark models are shown in Fig. (12) where the  $Z'$  boson has a decay width  $\sim 4$  GeV (7 MeV) for  $m_\chi = 0$  (75) GeV. For the  $m_\chi = 0$  case, the resonances reconstructed via both channels exhibit the  $Z'$  intrinsic width. However, for the  $m_\chi = 75$  GeV case,

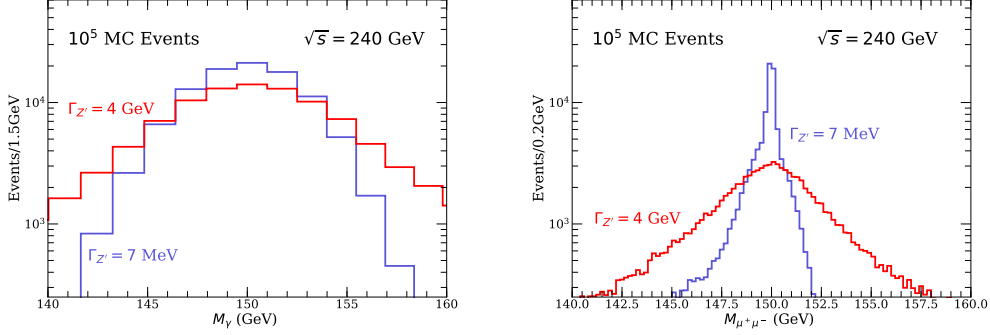


**Figure 12.** Left panel:  $M_\gamma$  distribution in  $e^+e^- \rightarrow \gamma Z' \rightarrow \bar{\chi}\chi\gamma$  in the CEPC  $H$ -mode, where  $M_\gamma = \sqrt{s - 2\sqrt{s}E_\gamma}$ . Right panel:  $M_{\mu^+\mu^-}$  distribution in  $e^+e^- \rightarrow \gamma Z' \rightarrow \mu^+\mu^-\gamma$  in the CEPC  $H$ -mode. We consider the vector coupling case (i.e.,  $g_A = 0$ ), where  $g_V^\chi = 1$  and  $g_V^f = 0.01$ . The  $Z'$  boson mass is fixed at  $M_{Z'} = 150$  GeV. We consider two different DM masses: (1)  $m_\chi = 0$  GeV so that the  $Z'$  boson has a large decay width  $\Gamma_{Z'} \simeq 4.0$  GeV; (2)  $m_\chi = 75$  GeV so that the  $Z'$  boson has a narrow width  $\Gamma_{Z'} \simeq 7.0$  MeV. Simulations in both channels are carried out with MadGraph and Delphes.

because the intrinsic  $Z'$  decay width is smaller than the resolution in the photon channel as well as in the di-muon channel, the reconstructed  $Z'$  peaks in both channels exhibit the widths due to detector resolutions. Thus, we select dimuon events in the invariant mass window  $M_{\mu\mu} \in (150 \pm 3)$  GeV for  $m_\chi < 75$  GeV, and  $M_{\mu\mu} \in (150 \pm 0.5)$  GeV for  $m_\chi > 75$  GeV.

In our  $Z'$  portal DM model, we assume that the  $Z'$  boson has a universal coupling to both charged leptons and to quarks. Thus, one expects a recoil signal arising from the  $Z'$  portal DM model in dark matter direct detection experiments that look for weakly interacting massive particles (WIMPs). Below we consider two different cases. First, we consider the case where the  $Z'$  boson couples both to SM fermions and to DM fermion via vector couplings; in this case, the dark matter direct detection cross section is dominated by the spin-independent (SI) cross section which is given by

$$\sigma_{n\chi}^{\text{SI}} = \sigma_{p\chi}^{\text{SI}} = \frac{9}{\pi} \frac{(g_V^f g_V^\chi \mu_{n\chi})^2}{M_{Z'}^4} \quad (5.2)$$

where  $\mu_{n\chi}$  is the reduced mass of the DM and nucleon. We also consider the case where the  $Z'$  boson couples both to SM fermions and to DM fermion via axial-vector couplings; in this case, the dark matter direct detection cross section is dominated by the spin-dependent (SD) cross section which is given by [51] [52]

$$\sigma_{n\chi}^{\text{SD}} = \sigma_{p\chi}^{\text{SD}} \simeq \frac{0.31}{\pi} \frac{(g_A^f g_A^\chi \mu_{n\chi})^2}{M_{Z'}^4}. \quad (5.3)$$

In our analysis, we assume that the  $Z'$  boson interacts with DM via an  $\mathcal{O}(1)$  coupling, and has a rather weak coupling strength with the SM sector. We consider two cases where



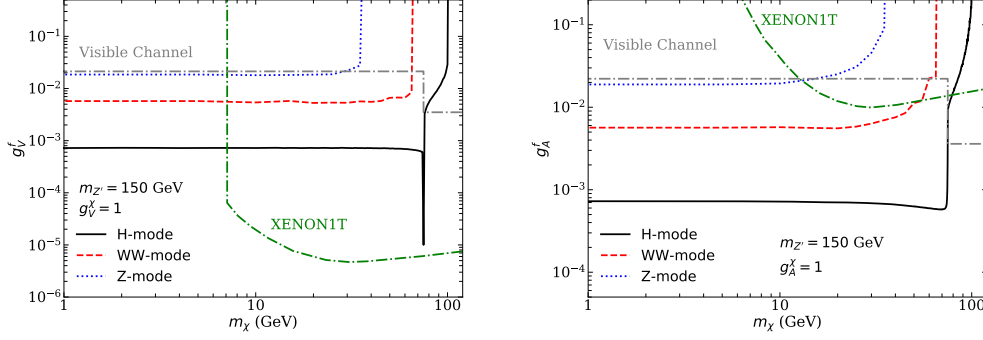


**Figure 13.** Expected CEPC limits on  $g_V^f$  (left), and on  $g_A^f$  (right), in the  $Z'$  portal DM model where  $M_{Z'} = 150$  GeV, from the monophoton channel  $e^+e^- \rightarrow \gamma Z' \rightarrow \gamma \bar{\chi}\chi$  in the three CEPC running modes. On the left (right) panel plot, only vector (axial-vector) couplings are assumed, with  $g_V^\chi = 1$  (left) and  $g_A^\chi = 1$  (right). Also shown are limits from  $e^+e^- \rightarrow \gamma Z' \rightarrow \gamma \mu^+\mu^-$  in the  $H$ -mode, from SI limit [53] (left) and SD limit [51] (right) in Xenon1T.

$Z'$  couples with fermions via only vector couplings, and via only axial-vector couplings. The left panel figure of Fig. (13) shows the 95% CL upper bound on  $g_V^f$  where  $g_V^\chi = 1$ , in the vector coupling only case; the right panel figure of Fig. (13) shows the 95% CL upper bound on  $g_A^f$  where  $g_A^\chi = 1$ , in the axial-vector coupling only case. For light dark matter mass, the monophoton channel in the  $H$ -mode has the best sensitivity in probing the gauge couplings between the 150 GeV  $Z'$  boson and the SM fermions for both vector and axial-vector cases, as shown in Fig. (13). CEPC can probe both  $g_V^f$  and  $g_A^f$  down to  $\sim 7 \times 10^{-4}$  for  $m_\chi < M_{Z'}/2 = 75$  GeV via monophoton searches. However, for  $m_\chi > 75$  GeV, the visible decays of the  $Z'$  boson become the better channel to study the  $Z'$  model considered where the monophoton channel quickly loses its sensitivity, as shown on both plots in Fig. (13). Interestingly, there is a sudden increase in the sensitivity in the monophoton channel when the dark matter mass approaches 75 GeV from below so that a very narrow dip structure is shown near  $m_\chi = 75$  GeV, in the vector coupling only case. There is also an increased sensitivity in the di-muon channel when  $m_\chi$  becomes larger than 75 GeV, due to the change of the detector cuts as the  $Z'$  width turns narrower for  $m_\chi$  crosses 75 GeV. We also compute the upper bound from Xenon1T experiment, including the SI limit [53] for the vector coupling case, and the SD limit [51] for the axial-vector coupling case. The Xenon1T limit is stronger than the CEPC limit for  $m_\chi \geq 5$  GeV in the vector only case. For the axial-vector only case, however, the CEPC limits are typically better than the current Xenon1T limits. We apply Xenon1T limits to the  $Z'$  portal DM models based on the assumption that the  $Z'$  boson couples to both charged leptons and quarks with equal coupling strength. If the  $Z'$  boson only interacts with electrons in the SM sector, the Xenon1T limits analyzed is no longer applicable.

We further study the constraints from the monophoton channel and from the di-muon channel to the two dimensional parameter space spanned by  $g_V^\chi$  and  $g_V^f$  in the vector coupling case where  $M_{Z'} = 150$  GeV and  $m_\chi = 50$  GeV, as shown in Fig. (14). The monopho-



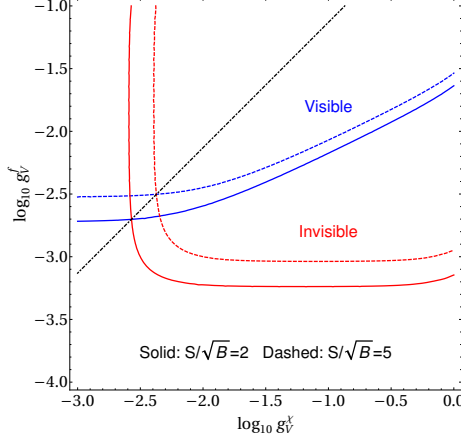


**Figure 14.** The CEPC sensitivity on the  $g_V^\chi$ - $g_V^f$  plane in the  $H$ -mode via the monophoton channel  $e^+e^- \rightarrow \gamma Z' \rightarrow \gamma \chi \chi$  (the invisible channel), and via the dimuon channel  $e^+e^- \rightarrow \gamma Z' \rightarrow \gamma \mu^+ \mu^-$  (the visible channel). We consider the vector coupling only case with  $M_{Z'} = 150$  GeV and  $m_\chi = 50$  GeV. The upper bounds in the visible (invisible) channel are shown in blue (red) lines assuming  $5.6 \text{ ab}^{-1}$  data in the  $H$ -mode; the solid (dashed) lines indicate the  $2 \sigma$  ( $5 \sigma$ ) reaches. The black dot-dashed line divides the parameter space into two regions: the invisible (visible) channel is the better channel in the region below (above) the black line. Here only di-muon events in the invariant mass window  $150 \pm 3$  GeV are selected.

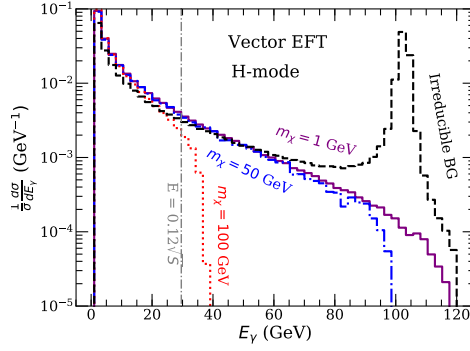
ton channel (invisible) usually provides a better constraint than the di-muon channel (the visible channel) in the parameter space  $g_V^\chi \gtrsim g_V^f$ , and vice versa.

## 6 DM effective operators

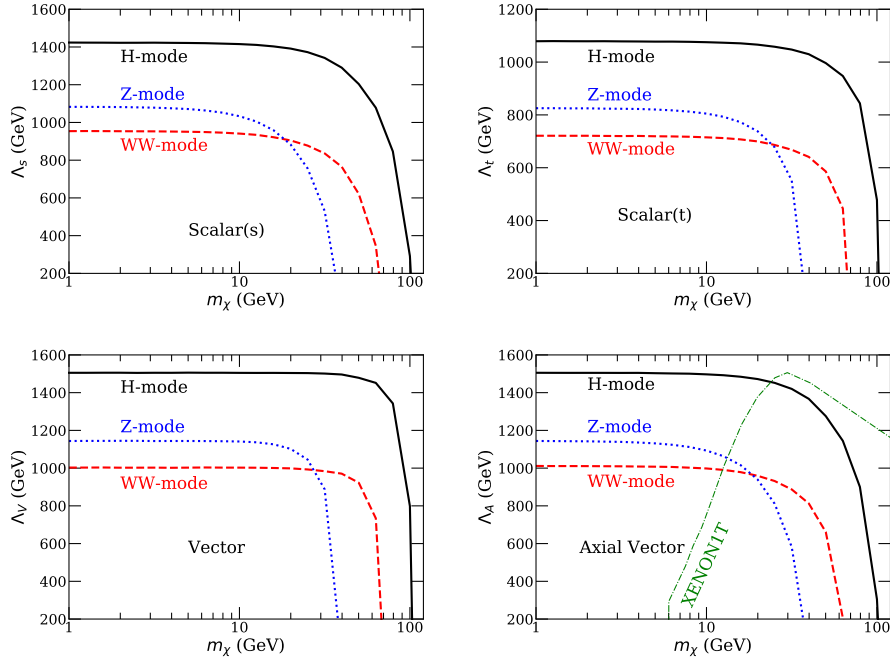
In this section, we study the potential CEPC constraints on DM effective operators. We consider the four effective operators as given in Eq. (2.3). Fig. (15) presents the normalized  $E_\gamma$  distribution at the CEPC in the  $H$ -mode for the process  $e^+e^- \rightarrow \chi \bar{\chi} \gamma$  in the vector operator case, along with the irreducible background  $e^+e^- \rightarrow \nu \bar{\nu} \gamma$  in the SM. Unlike the millicharged DM models and the  $Z'$  portal DM models, the monophoton energy spectrum in the vector operator case does not exhibit any peak structure in the hard photon region. Thus we use the basic detector cuts for the DM effective operator analysis in this section; for the  $H$ -mode, we further veto photon events with  $E_\gamma > 95$  GeV in addition to the basic detector cuts, to improve the CEPC sensitivity.

Fig. (16) shows the 95% C.L. lower bound on the new physics characteristic scale  $\Lambda$  as the function of the DM mass  $m_\chi$  for the four DM effective operators considered. We analyzed all the three running modes at the CEPC with the integrated luminosity as  $5.6 \text{ ab}^{-1}$  in the  $H$ -mode,  $2.6 \text{ ab}^{-1}$  in the  $WW$ -mode, and  $16 \text{ ab}^{-1}$  in the  $Z$ -mode. For all the four DM effective operators considered, the CEPC  $H$ -mode has the best sensitivity to  $\Lambda$  owing to the large production cross section; the  $Z$ -mode outperforms the  $WW$ -mode due to the larger integrated luminosity.

We further compute the dark matter detection limits on DM effective operators, under the assumption that DM couples to all SM fermions with universal couplings. For the



**Figure 15.** Normalized  $E_\gamma$  distribution in  $e^+e^- \rightarrow \chi\bar{\chi}\gamma$  for DM effective operator (the vector case), along with the SM irreducible background, in the CEPC  $H$ -mode.



**Figure 16.** Expected CEPC 95% CL lower bound on  $\Lambda$  with four different DM effective operators: the s-channel scalar interaction (upper left), the t-channel scalar interaction (upper right), the vector interaction (lower left), the axial-vector interaction (lower right). The SD limit from Xenon1T [51] is drawn for the axial-vector operator case, under the assumption that the effective operator coupling is universal.

vector, s-scalar, and t-scalar effective operators, the dominant contribution to the dark matter direct detection experiments is the SI cross section; for the axial-vector effective operator case, the dominant contribution to the dark matter direct detection experiments is the SD cross section. For the SD limit, we use

$$\sigma_{n\chi}^{\text{SD}} = \sigma_{p\chi}^{\text{SD}} = \frac{0.31}{\pi} \frac{\mu_{n\chi}^2}{\Lambda^4}; \quad (6.1)$$

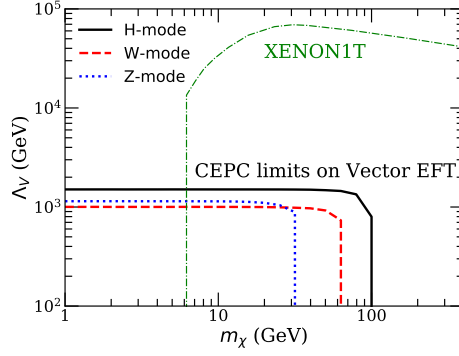


**Figure 17.** Comparison between CEPC sensitivity and SI limits from Xenon1T [53] under the assumption that the EFT couplings are universal for SM fermions.

for the SI limit, we use

$$\sigma_{n\chi}^{\text{SI}} = \sigma_{p\chi}^{\text{SI}} = \frac{9}{\pi} \frac{\mu_{n\chi}^2}{\Lambda^4} \quad (6.2)$$

where we have assumed that  $\Lambda$  takes the same value for all charged lepton flavors and for all quark flavors. The lower bound on  $\Lambda$  from the SD limit in Xenon1T experiment [51] is given in the lower-right panel plot in Fig. (16), for the axial-vector case. The lower bound on  $\Lambda$  from the SI limit in Xenon1T experiment [53] is given in Fig. (17), for the vector operator case. The constraints from SI limits on the two scalar operator cases are similar to the vector operator case. We note that the Xenon1T constraints presented here are no longer valid if DM couples only with electron via effective operators.

## 7 Detector cut optimization

We present a preliminary study on optimizing the detector cuts to enhance the CEPC capability in probing the parameter space of the dark matter models considered. To do so, we first divide the two dimensional signature space spanned by  $E_\gamma$  and  $\cos\theta_\gamma$  into 900 bins: 30 bins both in  $(0.12\sqrt{s} < E_\gamma < E_\chi^m)$  and in  $(-0.99 < \cos\theta_\gamma < 0.99)$ , for the monophoton channel at CEPC. In each of the 900 bins, we compute the signal cross section in the dark matter models  $\sigma_{\text{NP}}^i$ , and the SM cross section  $\sigma_{\text{BG}}^i$ ; we further sort the bins according to  $r^i \equiv \sigma_{\text{NP}}^i/\sigma_{\text{BG}}^i$  in descending order so that the first bin has the largest signal to background ratio. We then take the first  $n$  bins in the list to compute the 95% CL upper bound and determine the  $n$  value that leads to the best upper bound. We refer to this as the “optimized cut” hereafter. For the millicharged DM model in the CEPC  $H$ -mode, we find that typically  $n \simeq 20$  (700) for the very low (very high) dark matter mass.

Fig. (18) shows the new limits on millicharge in the CEPC  $H$ -mode if we use the optimized cuts. The improvement is significant in the low DM mass regions. In particular, the expected upper bound on  $\varepsilon$  goes from  $\sim 0.03$  to  $\sim 0.02$  for  $m_\chi = 0.1$  GeV.

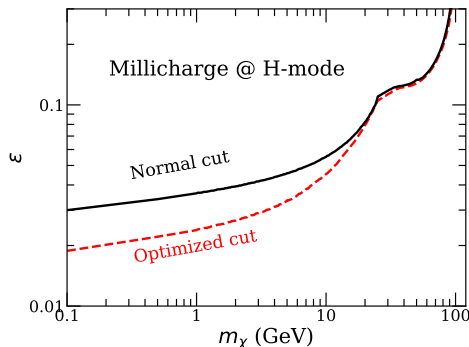


**Figure 18.** Expected 95% CL upper bound on millicharge analyzed with the “optimized” cuts, and with the cuts used previously for millicharged DM models.

## 8 Summary

In this work, we investigate the capability of CEPC in probing millicharged DM models,  $Z'$  portal DM models, and DM effective operators, by mainly using the monophoton channel. We propose a set of detector cuts which are found to efficiently suppress various background events and to improve the signal significance for the DM models considered.

For the millicharged DM models, the CEPC will probe the vast parameter space that is not constrained by previous collider experiments for  $\mathcal{O}(1) - 100$  GeV DM. The CEPC  $Z$ -mode with  $16 \text{ ab}^{-1}$  has a better sensitivity than the other two running modes in the millicharged DM mass range  $m_\chi \lesssim 40$  GeV, beyond which the  $H$ -mode dominates the reach. For  $m_\chi \simeq 5$  (50) GeV, a new leading upper bound on millicharge  $\varepsilon \lesssim 0.02$  (0.1) is expected at CEPC. We further carry out an investigation on optimizing the detector cuts to constrain the millicharge; we found a significant improvement in the limits for low mass millicharged DM, by selecting only the high signal-to-background regions in the signature space.

For the  $Z'$  portal DM model where  $M_{Z'} = 150$  GeV, we find that CEPC can explore the coupling down to  $g^f \simeq 7 \times 10^{-4}$  for  $g^\chi = 1$  in low DM mass region for both vector and axial vector couplings. An increased sensitivity on  $g_V^f$  is observed for  $m_\chi \simeq M_{Z'}/2$ . We compare the constraining power of the monophoton channel with the  $Z'$  visible decay channel and find that the visible channel is usually the better channel in parameter space where  $g^f \gtrsim g^\chi$ , and vice versa. For DM effective operators, the best constraints on the energy scale  $\Lambda$  come from the CEPC  $H$ -mode in which  $\Lambda$  up to  $\simeq 1500$  GeV in s-scalar, axial vector and vector effective operators and  $\simeq 1100$  GeV in t-scalar effective operators can be reached.

A complementary study on CEPC and dark matter direct detection limits from Xenon1T is carried out for  $Z'$  portal and DM effective operators. For DM in the mass range 10-100 GeV, Xenon1T can cast a limit as good as CEPC or better assuming universal fermion couplings. CEPC provides better limits than the Xenon1T experiment, for GeV or sub-GeV dark matter particles, or in the case where DM only couples to electrons. We did

not study the direct detection signal in Xenon1T for the millicharged dark matter particle, because it is likely to be absorbed in rock above the underground labs hosting dark matter direct detection experiments, for the millicharge of interest at CEPC searches.

## Acknowledgments

We thank Zihao Xu for discussions. The work is supported in part by the National Natural Science Foundation of China under Grant Nos. 11775109, U1738134 and 11805001, and by the National Recruitment Program for Young Professionals.

## References

- [1] Y. Akrami *et al.* [Planck Collaboration], arXiv:1807.06205 [astro-ph.CO].
- [2] [CEPC Study Group], arXiv:1811.10545 [hep-ex].
- [3] H. Baer *et al.*, arXiv:1306.6352 [hep-ph].
- [4] M. Bicer *et al.* [TLEP Design Study Working Group], JHEP **1401**, 164 (2014) doi:10.1007/JHEP01(2014)164 [arXiv:1308.6176 [hep-ex]].
- [5] H. Abramowicz *et al.* [CLIC Detector and Physics Study Collaboration], arXiv:1307.5288 [hep-ex].
- [6] A. Birkedal, K. Matchev and M. Perelstein, Phys. Rev. D **70**, 077701 (2004) doi:10.1103/PhysRevD.70.077701 [hep-ph/0403004].
- [7] P. Konar, K. Kong, K. T. Matchev and M. Perelstein, New J. Phys. **11**, 105004 (2009) doi:10.1088/1367-2630/11/10/105004 [arXiv:0902.2000 [hep-ph]].
- [8] P. J. Fox, R. Harnik, J. Kopp and Y. Tsai, Phys. Rev. D **84**, 014028 (2011) doi:10.1103/PhysRevD.84.014028 [arXiv:1103.0240 [hep-ph]].
- [9] C. Bartels, M. Berggren and J. List, Eur. Phys. J. C **72**, 2213 (2012) doi:10.1140/epjc/s10052-012-2213-9 [arXiv:1206.6639 [hep-ex]].
- [10] Y. J. Chae and M. Perelstein, JHEP **1305**, 138 (2013) doi:10.1007/JHEP05(2013)138 [arXiv:1211.4008 [hep-ph]].
- [11] H. Dreiner, M. Huck, M. Krämer, D. Schmeier and J. Tattersall, Phys. Rev. D **87**, no. 7, 075015 (2013) doi:10.1103/PhysRevD.87.075015 [arXiv:1211.2254 [hep-ph]].
- [12] Z. H. Yu, Q. S. Yan and P. F. Yin, Phys. Rev. D **88**, no. 7, 075015 (2013) doi:10.1103/PhysRevD.88.075015 [arXiv:1307.5740 [hep-ph]].
- [13] Z. H. Yu, X. J. Bi, Q. S. Yan and P. F. Yin, Phys. Rev. D **90**, no. 5, 055010 (2014) doi:10.1103/PhysRevD.90.055010 [arXiv:1404.6990 [hep-ph]].
- [14] N. Wan, M. Song, G. Li, W. G. Ma, R. Y. Zhang and J. Y. Guo, Eur. Phys. J. C **74**, no. 12, 3219 (2014) doi:10.1140/epjc/s10052-014-3219-2 [arXiv:1403.7921 [hep-ph]].
- [15] M. Karliner, M. Low, J. L. Rosner and L. T. Wang, Phys. Rev. D **92**, no. 3, 035010 (2015) doi:10.1103/PhysRevD.92.035010 [arXiv:1503.07209 [hep-ph]].
- [16] K. Harigaya, K. Ichikawa, A. Kundu, S. Matsumoto and S. Shirai, JHEP **1509**, 105 (2015) doi:10.1007/JHEP09(2015)105 [arXiv:1504.03402 [hep-ph]].

- [17] Q. H. Cao, Y. Li, B. Yan, Y. Zhang and Z. Zhang, Nucl. Phys. B **909**, 197 (2016) doi:10.1016/j.nuclphysb.2016.05.010 [arXiv:1604.07536 [hep-ph]].
- [18] Q. F. Xiang, X. J. Bi, Q. S. Yan, P. F. Yin and Z. H. Yu, Phys. Rev. D **95**, no. 7, 075037 (2017) doi:10.1103/PhysRevD.95.075037 [arXiv:1610.03372 [hep-ph]].
- [19] C. Cai, Z. H. Yu and H. H. Zhang, Nucl. Phys. B **921**, 181 (2017) doi:10.1016/j.nuclphysb.2017.05.015 [arXiv:1611.02186 [hep-ph]].
- [20] C. Cai, Z. H. Yu and H. H. Zhang, Nucl. Phys. B **924**, 128 (2017) doi:10.1016/j.nuclphysb.2017.09.007 [arXiv:1705.07921 [hep-ph]].
- [21] Q. F. Xiang, X. J. Bi, P. F. Yin and Z. H. Yu, Phys. Rev. D **97**, no. 5, 055004 (2018) doi:10.1103/PhysRevD.97.055004 [arXiv:1707.03094 [hep-ph]].
- [22] J. W. Wang, X. J. Bi, Q. F. Xiang, P. F. Yin and Z. H. Yu, Phys. Rev. D **97**, no. 3, 035021 (2018) doi:10.1103/PhysRevD.97.035021 [arXiv:1711.05622 [hep-ph]].
- [23] M. He, X. G. He and C. K. Huang, Int. J. Mod. Phys. A **32**, no. 23n24, 1750138 (2017) doi:10.1142/S0217751X1750138X [arXiv:1701.08614 [hep-ph]].
- [24] M. He, X. G. He, C. K. Huang and G. Li, JHEP **1803**, 139 (2018) doi:10.1007/JHEP03(2018)139 [arXiv:1712.09095 [hep-ph]].
- [25] J. Liu, L. T. Wang, X. P. Wang and W. Xue, Phys. Rev. D **97**, no. 9, 095044 (2018) doi:10.1103/PhysRevD.97.095044 [arXiv:1712.07237 [hep-ph]].
- [26] M. Jin and Y. Gao, Eur. Phys. J. C **78**, no. 8, 622 (2018) doi:10.1140/epjc/s10052-018-6093-5 [arXiv:1712.02140 [hep-ph]].
- [27] K. Kadota and A. Spray, JHEP **1902**, 017 (2019) doi:10.1007/JHEP02(2019)017 [arXiv:1811.00560 [hep-ph]].
- [28] Z. Liu and Y. Zhang, Phys. Rev. D **99**, no. 1, 015004 (2019) doi:10.1103/PhysRevD.99.015004 [arXiv:1808.00983 [hep-ph]].
- [29] T. Hahn, Comput. Phys. Commun. **140** (2001) 418 doi:10.1016/S0010-4655(01)00290-9 [hep-ph/0012260].
- [30] T. Hahn and M. Perez-Victoria, Comput. Phys. Commun. **118** (1999) 153 doi:10.1016/S0010-4655(98)00173-8 [hep-ph/9807565].
- [31] Shuzheng Wang, “Study on the performance of simulated CEPC high granularity electromagnetic calorimeter-energy, position resolution and linear range”, master thesis, 2017
- [32] S. Davidson, S. Hannestad and G. Raffelt, JHEP **0005**, 003 (2000) doi:10.1088/1126-6708/2000/05/003 [hep-ph/0001179].
- [33] D. E. Soper, M. Spannowsky, C. J. Wallace and T. M. P. Tait, Phys. Rev. D **90**, no. 11, 115005 (2014) doi:10.1103/PhysRevD.90.115005 [arXiv:1407.2623 [hep-ph]].
- [34] G. Magill, R. Plestid, M. Pospelov and Y. D. Tsai, Phys. Rev. Lett. **122**, no. 7, 071801 (2019) doi:10.1103/PhysRevLett.122.071801 [arXiv:1806.03310 [hep-ph]].
- [35] S. D. McDermott, H. B. Yu and K. M. Zurek, Phys. Rev. D **83**, 063509 (2011) doi:10.1103/PhysRevD.83.063509 [arXiv:1011.2907 [hep-ph]].
- [36] S. L. Dubovsky, D. S. Gorbunov and G. I. Rubtsov, JETP Lett. **79**, 1 (2004) [Pisma Zh. Eksp. Teor. Fiz. **79**, 3 (2004)] doi:10.1134/1.1675909 [hep-ph/0311189].

- [37] J. M. Cline, Z. Liu and W. Xue, Phys. Rev. D **85**, 101302 (2012) doi:10.1103/PhysRevD.85.101302 [arXiv:1201.4858 [hep-ph]].
- [38] A. D. Dolgov, S. L. Dubovsky, G. I. Rubtsov and I. I. Tkachev, Phys. Rev. D **88**, no. 11, 117701 (2013) doi:10.1103/PhysRevD.88.117701 [arXiv:1310.2376 [hep-ph]].
- [39] J. D. Bowman, A. E. E. Rogers, R. A. Monsalve, T. J. Mozdzen and N. Mahesh, Nature **555**, no. 7694, 67 (2018) doi:10.1038/nature25792 [arXiv:1810.05912 [astro-ph.CO]].
- [40] J. B. Muñoz and A. Loeb, Nature **557**, no. 7707, 684 (2018) doi:10.1038/s41586-018-0151-x [arXiv:1802.10094 [astro-ph.CO]].
- [41] A. Berlin, D. Hooper, G. Krnjaic and S. D. McDermott, Phys. Rev. Lett. **121**, no. 1, 011102 (2018) doi:10.1103/PhysRevLett.121.011102 [arXiv:1803.02804 [hep-ph]].
- [42] R. Barkana, N. J. Outmezguine, D. Redigolo and T. Volansky, Phys. Rev. D **98**, no. 10, 103005 (2018) doi:10.1103/PhysRevD.98.103005 [arXiv:1803.03091 [hep-ph]].
- [43] T. R. Slatyer and C. L. Wu, Phys. Rev. D **98**, no. 2, 023013 (2018) doi:10.1103/PhysRevD.98.023013 [arXiv:1803.09734 [astro-ph.CO]].
- [44] E. D. Kovetz, V. Poulin, V. Gluscevic, K. K. Boddy, R. Barkana and M. Kamionkowski, Phys. Rev. D **98**, no. 10, 103529 (2018) doi:10.1103/PhysRevD.98.103529 [arXiv:1807.11482 [astro-ph.CO]].
- [45] K. K. Boddy, V. Gluscevic, V. Poulin, E. D. Kovetz, M. Kamionkowski and R. Barkana, Phys. Rev. D **98**, no. 12, 123506 (2018) doi:10.1103/PhysRevD.98.123506 [arXiv:1808.00001 [astro-ph.CO]].
- [46] D. Wadekar and G. R. Farrar, arXiv:1903.12190 [hep-ph].
- [47] R. de Putter, O. Doré, J. Gleyzes, D. Green and J. Meyers, Phys. Rev. Lett. **122**, no. 4, 041301 (2019) doi:10.1103/PhysRevLett.122.041301 [arXiv:1805.11616 [astro-ph.CO]].
- [48] J. de Favereau *et al.* [DELPHES 3 Collaboration], JHEP **1402**, 057 (2014) doi:10.1007/JHEP02(2014)057 [arXiv:1307.6346 [hep-ex]].
- [49] J. Alwall *et al.*, JHEP **1407**, 079 (2014) doi:10.1007/JHEP07(2014)079 [arXiv:1405.0301 [hep-ph]].
- [50] T. Sjostrand, S. Mrenna and P. Z. Skands, Comput. Phys. Commun. **178**, 852 (2008) doi:10.1016/j.cpc.2008.01.036 [arXiv:0710.3820 [hep-ph]].
- [51] E. Aprile *et al.* [XENON Collaboration], arXiv:1902.03234 [astro-ph.CO].
- [52] A. Boveia *et al.*, arXiv:1603.04156 [hep-ex].
- [53] E. Aprile *et al.* [XENON Collaboration], Phys. Rev. Lett. **121**, no. 11, 111302 (2018) doi:10.1103/PhysRevLett.121.111302 [arXiv:1805.12562 [astro-ph.CO]].